PCCP

PAPER

View Article Online
View Journal | View Issue

Cite this: *Phys. Chem. Chem. Phys.*, 2023, **25**, 31346

Li intercalation in 2D iron phosphate synthesized from the partial dehydration and deprotonation of vivianite†

Ryo Yamane, * Hongyi Li, Tetsu Ichitsubo and Kazumasa Sugiyama

Received 29th May 2023,
Accepted 6th November 2023

DOI: 10.1039/d3cp02463f

rsc.li/pccp

This study focuses on the cation intercalation of structurally unique compounds synthesized from the partial dehydration and deprotonation of coordinated water molecules in hydrous materials. Partial dehydration can potentially result in hydrous materials with a porous nature, which maintains the parent structure of the material, and deprotonation causes oxidation in the hydrous materials. Li-intercalation experiments were conducted on the hydrous iron(II) phosphate mineral, vivianite ($Fe_3^{2+}(PO_4)_2{\cdot}8H_2O$), and its oxidized and partially dehydrated product, santabarbaraite. Vivianite comprises two-dimensional $Fe_3(PO_4)_2$ sheets and coordinated water molecules. The oxidation progress of the Fe^{2+} of vivianite increased cathodic capacities up to 156 mA h g^{-1}. The Li-intercalation reaction rate increased significantly owing to dehydration because the partial dehydration of vivianite created structural space for the diffusion of Li^+. Furthermore, X-ray diffraction measurements revealed that Li intercalation did not cause the formation of byproducts.

1. Introduction

Fe-based polyanionic oxides are promising compounds for energy-storage applications because of their low cost and environmental sustainability.[1] Hydrous materials are commonly used as precursors for the synthesis of polyanionic oxides. Incorporated water (H_2O) molecules are typically removed in the synthetic processes to form compounds that are characterized by three-dimensional (3D) linkages, such as olivine-type $LiFePO_4$.[1] Although rarely investigated, partially dehydrated polyanionic oxides (PDPOs) can have an appropriate porous nature and oxidation states for cation intercalation. For example, if a unique structure is inherited from the parent hydrous material of PDPOs, dehydration increases the porosity of the structure of PDPO.[2] When a central metal atom coordinates to H_2O molecules, oxidation can occur *via* a concerted reaction between the oxidation of the metal atom and deprotonation of the H_2O molecules to hydroxyl (OH) groups.[3] This concerted reaction is feasible for Fe-based PDPOs because of the comparable stability of Fe^{2+} and Fe^{3+} ($Fe^{3+} + e^- \rightarrow Fe^{2+}$, E° = +0.77 V *vs.* SHE[4]). The H_2O molecules or OH groups of PDPOs hinder the characteristic 3D linkages of polyanionic oxides, and OH decreases the metal/polyanion atomic ratio.

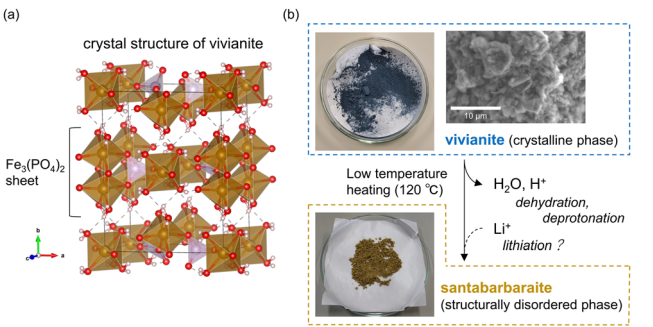

Fig. 1 (a) Crystal structure of VV ($Fe_3(PO_4)_2{\cdot}8H_2O$).‡ (b) Schematic representation of the phase relationship between VV and SB ($Fe_3(PO_4)_2(OH)_3{\cdot}1.4H_2O$), with photos of the synthesized samples, and a scanning electron microscope image of the synthesized VV.

For example, in iron phosphates, the Fe-to-PO_4 ratio is 3 : 2, but in the presence of OH, the ratio changes to 1 : 1. These characteristics can be leveraged to generate novel types of polyanionic oxide structures with structural dimensions lower than those of normal Fe-based polyanion oxides characterized by 3D linkages.

Therefore, a hydrous iron(II) phosphate, vivianite (VV; $Fe_3^{2+}(PO_4)_2{\cdot}8H_2O$),[5] was investigated (Fe can be substituted by Co and Ni).[6] VV comprises two-dimensional (2D) $Fe_3(PO_4)_2$

Institute for Materials Research, Tohoku University, Sendai 980-8577, Japan.
E-mail: ryo.yamane.c2@tohoku.ac.jp

† Electronic supplementary information (ESI) available. See DOI: https://doi.org/10.1039/d3cp02463f

‡ Crystal structures were drawn using VESTA developed by Momma and Izumi (2011).[14]

sheets connected *via* relatively weak hydrogen bonds between the coordinated H_2O molecules (Fig. 1(a)).† [7] The Fe^{2+} ions in VV can be partially oxidized *via* the deprotonation of coordinated water molecules:[8–11]

$$2[Fe^{2+} - H_2O] + \frac{1}{2}O_2 \rightarrow 2[Fe^{3+} - OH] + H_2O.$$

VV is further oxidized upon heating, causing partial dehydration. Upon heating, the parent VV converts to a structurally disordered and partially dehydrated phase of santabarbaraite (SB) at approximately 120 °C.[12]

This study demonstrates the favorable electrochemical properties of partially dehydrated SB compared to those of VV. The favorable behavior of Li intercalation in SB would be a breakthrough for further electrochemical studies focusing on PDPOs, thus enabling the discovery of novel structural characteristics and new roles of H_2O ligands in the formation of PDPOs.

2. Experimental

2.1 Synthesis of VV and SB

VV samples were synthesized using the method described by Chiba *et al.*[13] Diammonium phosphate (0.60 g, Wako Pure Chemical Industries Ltd, 99.0%) and ferrous sulfate heptahydrate (1.80 g, FUJIFILM Wako Pure Chemical Corp., 99.0%) were dissolved in distilled H_2O (90 mL). The mixture was stirred for 1 h at 470 rpm using a hot plate stirrer (DLAB MS-H280-Pro) under atmospheric conditions. The obtained precipitate was washed with distilled H_2O and air dried for 24 h. The obtained VV had a deep blue color (Fig. 1(b)). The precipitate had a light blue color if washed with ethanol and dried immediately by vacuum filtration. Additionally, the grain size of the sample was controlled from a few to tens of micrometers, with grain sizes < 10 μm used for experimentation (Fig. 1(b)), by changing the amount of H_2O (solvent). SB was synthesized by heating the obtained VV at 120 °C for 2 h in air. We also synthesized SB* by heating the sample at 500 °C for 2 h. This sample was used in the X-ray absorption near-edge structure (XANES) analysis for comparison with SB. The weight loss from the synthesized VV to the SB corresponded to the dehydration of 3.6 H_2O molecules based on our preliminary thermogravimetric measurements (Fig. S1, ESI†). Therefore, the chemical composition of SB was approximately $Fe_3(PO_4)_2(OH)_3{\cdot}1.4H_2O$.

2.2 Preparation of cathode electrodes

An ordinary two-electrode cell (SB2A, EC-FRONTIER Co., Ltd) was employed for the Li-intercalation test of iron phosphates (*i.e.*, partially oxidized VV and SB). The active material applied on Al foil (30 μm) was a mixture of iron phosphate, carbon black (Super C65, Hohsen Corp.), and polyvinylidene fluoride (5 mass% in *N*-methylpyrrolidone, Kureha Corporation) at a weight ratio of 8 : 1 : 1. The cathode electrode using VV was vacuum dried for 48 h at 30 °C after mixing the active substances to remove the *N*-methylpyrrolidone solvent. The vacuum-drying conditions were changed to 24 h at 120 °C for the cathode electrode using SB. The active material loadings of VV and SB were 3.03 and 2.74 mg cm^{-2}, respectively.

2.3 X-ray diffraction

The synthesized VV and SB were characterized *via* powder X-ray diffraction (XRD) using a Rigaku Ultima III diffractometer with Co-Kα radiation and Bragg–Brentano geometry. The XRD patterns of the Li-intercalated samples were measured using a Rigaku SmartLab diffractometer with Mo-Kα radiation. The Li-intercalated samples and Al foil were first washed with tetrahydrofuran to remove the absorbed electrolyte and then dried in an Ar atmosphere. After removing the Al foil, the powdered samples were encapsulated in a glass capillary tube, with an outer diameter and thickness of 0.5 and 0.01 mm, respectively. The XRD patterns of the encapsulated samples before and after Li intercalation were measured using transmission geometry. In addition, XRD patterns were simulated using the VESTA program.[14]

2.4 X-ray absorption near-edge structure

XANES spectra were obtained around the Fe K-absorption edges to investigate the oxidation states of the synthesized iron phosphates. The analysis was performed at the Institute of Material Structure Science, High Energy Accelerator Research Organization (KEK) in Tsukuba, Japan. A transmission method was employed, and the samples were pressed into pellets with a diameter of 10 mm using boron nitride (200 mg). We estimated the Fe *K*-absorption edges of the samples using the half-energy positions of the maximum and minimum absorptions.

2.5 Li-intercalation test

Two-electrode cells were assembled in an Ar-filled glovebox using the composite electrode as the working electrode, an Li metal plate (Honjo Metal Co. Ltd) as the quasi-reference/counter electrode, and a commercial electrolyte (Merck KGaA) of 1 M $LiPF_6$ in an ethylene carbonate and dimethyl carbonate solution (1 : 1 volume ratio). In the reaction experiments, constant-current–constant-voltage (CC–CV) discharging and charging processes were employed, with cut-off voltages of 2.0 and 4.5 V for discharging and charging, respectively. A potentiostat (VMP-3, Bio-Logic SAS) was used in this experiment. In addition, discharge–charge cycle tests were conducted using a battery charge/discharge system (HJ1001SD8, HOKUTO DENKO CORPORATION) under the CC condition with cut-off voltages of 2.0 and 4.0 V for discharging and charging, respectively. Before Li intercalation, the samples were referred to as ''pristine'' in this study. The charge/discharge rate was 0.025C (1C: 225 mA g^{-1}) in these Li-intercalation tests.

3. Results and discussion

The XANES spectra of the samples are shown in Fig. 2. The XANES spectrum of phosphophyllite (or $FeZn_2(PO_4)_2{\cdot}4H_2O$) was measured as a standard of hydrous iron(II) phosphate. A spectrum of the SB* is also shown to compare its Fe oxidation

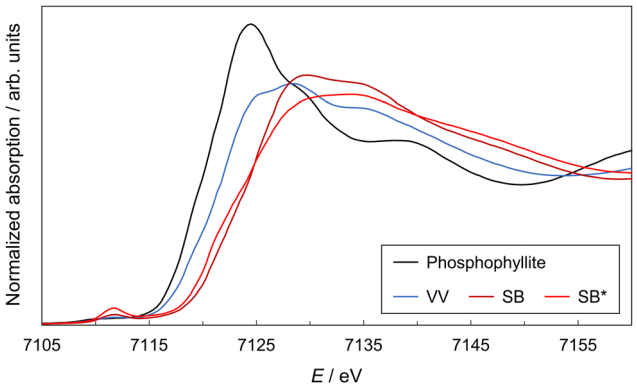

Fig. 2 X-ray absorption near-edge structure spectra of VV, SB, and SB*. A spectrum of phosphophyllite ($FeZn_2(PO_4)_2{\cdot}4H_2O$) is shown as the standard hydrous iron(II) phosphate.

state with that of SB. The Fe K-absorption edges of phosphophyllite and VV were 7120.1 and 7121.1 eV, respectively. This shift in the absorption edge is due to the partially oxidized state of VV. An absorption edge shift from 7121.1 to 7123.6 eV was observed between the VV and SB. Conversely, no significant indication of oxidation progress, which was completed at 120 °C, was observed between the SB and SB* (absorption edge of SB*: 7122.7 eV). The results of the Li-intercalation tests are presented in Fig. 3(a), which show the results of the CC–CV discharging process using the electrodes of VV and SB (#1 and #2, respectively). The result of the CC–CV discharging and charging processes using SB is shown as #3. The retention time of the CV discharging process was 72 h for samples #1 and #2 and 24 h for sample #3. The cathodic capacities of #2 and #1 were 156 and 70.9 mA h g^{-1}, respectively. This difference is because the Fe^{3+} content in SB was higher than that in VV. Notably, VV immediately reached a cut-off voltage of 2.0 V in the CC discharging process. This result indicated a significantly lower reaction rate for Li intercalation in VV. The reaction rate is controlled by the electron conductivity and Li^+ diffusivity of iron phosphates. The electron conductivity of VV is higher than that of SB,§ [15] because SB has a disordered structure. However, SB has more space for Li^+ diffusivity owing to the loss of H_2O molecules *via* dehydration. The higher reaction rate of SB was attributed to its Li^+ diffusivity. Therefore, SB is a more suitable active material than VV in terms of capacity and reaction rate for Li intercalation. Additionally, SB shows Li deintercalation in the voltage–capacity curve of sample #3 in Fig. 3(a). It should be noted that #2 and #3 showed different voltages and capacities during discharging, although their durations in the CV process differed. These differences were reproduced in other electrodes made of synthesized SB materials that differed from those used in #2 and 3 (the results of the Li-intercalation tests of these samples are shown in Fig. S2 as #4 and #5, ESI†). Therefore, the inhomogeneity of the oxidation and dehydration states of the

§ Electrical conductivity of SB at 297 K was estimated from the extrapolation of data measured at >110 °C.[15]

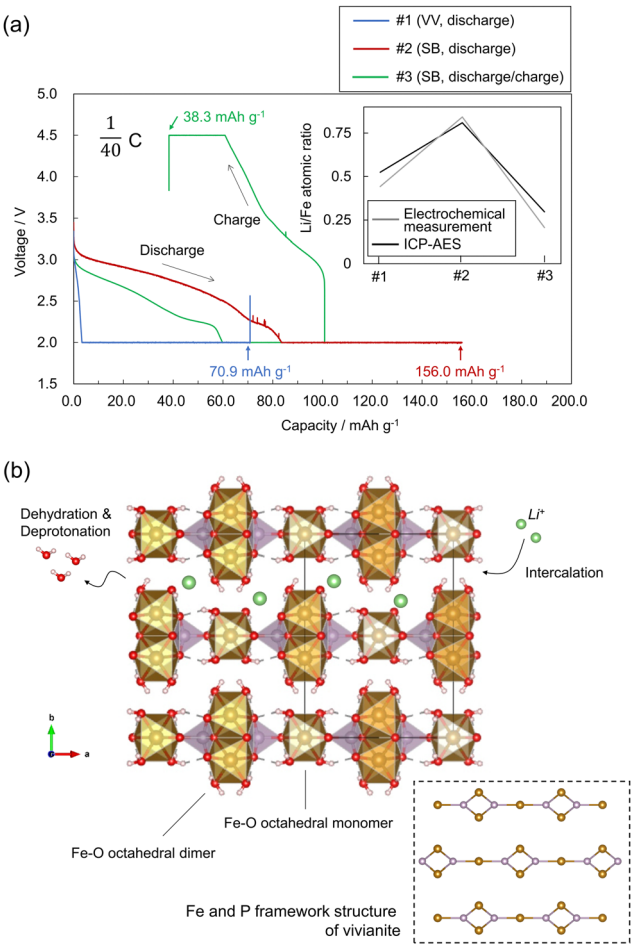

Fig. 3 (a) Discharge/charge curves of VV and SB. The results of the constant-current–constant-voltage (CC–CV) discharging process using VV- and SB-electrodes are shown as samples #1 and #2, respectively. The results of the CC–CV discharging and charging processes using the SB-electrode are shown as sample #3. The charge/discharge rate was 0.025C. Inset shows the Fe/Li atomic ratio of the three samples that was estimated using electrochemical measurements and inductively coupled plasma atomic emission spectroscopy (ICP-AES) analysis. (b) Schematic of Li intercalation into the crystal structure of VV. A framework structure of VV is described in the bottom right using Fe and P atoms.

samples causes the observed differences between the samples. However, the cause of this inhomogeneity remains unclear.

The capacity of the electrode of VV reached 70.9 mA h g^{-1} in the CV process following the CC process, even though it had a significantly lower Li-intercalation reaction rate than the electrode of SB. Li^+ accumulated between the 2D-$Fe_3(PO_4)_2$ sheets in the crystal structure of VV (Fig. 3(b)). The accumulated amounts of Li^+ in samples #1, #2, and #3 were evaluated using electrochemical measurements and inductively coupled plasma atomic emission spectroscopy (ICP-AES) analysis (inset of Fig. 3(a)). The amount of Li^+ is shown as an atomic ratio compared to the amount of Fe atoms. The results of the evaluations were consistent, with approximately 80% of the Fe atoms in SB reduced by Li intercalation. Therefore, at least 80% of the Fe ions existed as Fe^{3+} in the 120 °C heated sample.

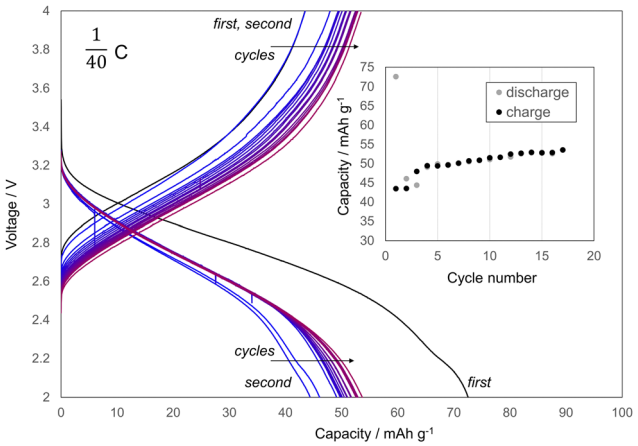

Fig. 4 Discharge–charge cycle with #4. The charge/discharge rate was 0.025C. The inset shows corresponding capacity retention plots.

This result is consistent with that of the XANES measurement, in which the oxidation of SB was nearly complete at 120 °C. The results of the discharge–charge cycle tests using the SB electrode (#4) are shown in Fig. 4. The Coulombic efficiency, which is the ratio of the discharge capacity to the charge capacity, improved with cycling, and the reversible capacity was gradually increased to greater than 50 mA h g^{-1}. This increase in the reversible capacity implies that structural relaxation occurred during cycling, which improved the Li^+ de-/intercalation in SB.

A comparison between the XRD patterns of VV before and after Li intercalation is shown in Fig. 5(a), where the sample after Li intercalation corresponds to sample #1 in Fig. 3(a). Besides the Bragg peaks derived from VV, no new peaks were observed. Peak shifts toward lower angles were observed. A shift of the 020 peak at around 6° in 2θ indicated that the separation of $Fe_3(PO_4)_2$ sheets, which correspond to the half-length of the *b*-axis, increased from 6.57 to 6.72 Å *via* Li intercalation (estimated from the peak top position of the 020 peak). This was an increase of approximately 2%. Furthermore, Li intercalation caused structural disorder, which was observed by the halo in the XRD pattern (Fig. 5(a)). This halo is in good agreement with the XRD patterns of #2 (discharged SB in Fig. 3(a)) shown in Fig. 5(b). The inset of Fig. 5(a) shows a comparison between the XRD patterns of #1 and #2. Given that the halo patterns reflect the atomic arrangements of the samples, this agreement indicates that the two disordered structures obtained in different ways, namely through Li intercalation and dehydration/deprotonation, are similar. Thus, neither structure significantly deviated from its parent structure. A comparison between the XRD patterns of SB before and after Li intercalation is shown in Fig. 5(b). No significant change indicating the formation of byproducts could be observed. However, a change was observed in a bump in the 2θ region of 10–15°. The bump appeared to include two peaks, marked as (1) and (2). The coherent scattering intensity of the structurally disordered material can be expressed using the Debye scattering equation.[16–19] In this equation, the oscillation of a scattering pattern is represented by the combination of

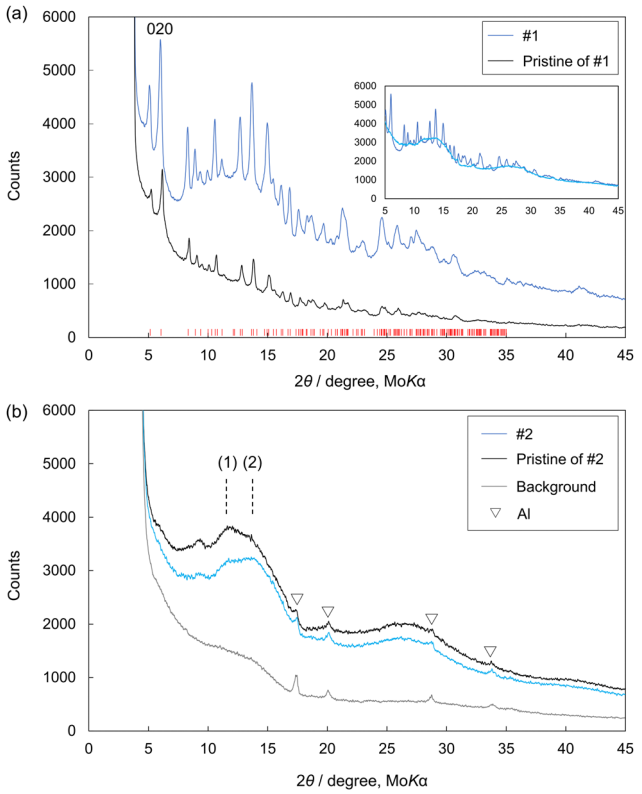

Fig. 5 (a) Comparison of the X-ray diffraction (XRD) patterns of #1 (discharged VV shown in Fig. 3(a)) and its pristine form. The red ticks show the Bragg peak positions of VV. In the inset, the XRD pattern of #2 (discharged SB shown in Fig. 3(a)) shown in (b) is overlaid on the XRD pattern of #1. (b) Comparison of the XRD patterns of #2 and its pristine form. Bragg peaks marked with ▽ are from Al in a measurement cell.

$\sin(Qr)/Qr$ for each atom pair, where *r* is the atomic distance of an atom pair, and *Q* is $4\pi\sin(\theta)/\lambda$. The *r* values were approximately 4.5 and 3.5 Å for peaks (1) and (2), respectively. The VV structure, on the other hand, has a characteristic dispersion of atomic correlations in the simulated pair distribution functions *g*(*r*). Atomic correlations of 4.7 Å correspond to the cell length of the *c*-axis, which is the in-plane direction of the 2D-$Fe_3(PO_4)_2$

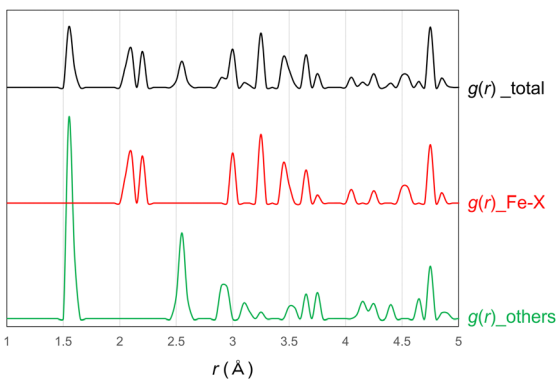

Fig. 6 Pair distribution function of VV (total) and its partial pair distribution functions of Fe–X (Fe–Fe, Fe–P, and Fe–O) and others (P–P, P–O, and O–O). The contribution from H is ignored.

sheet, and shorter atomic correlations appear in lower 3.7 Å. The $g(r)$ is shown with the ''total'' calculated atom pairs, and the $g(r)$ values of ''Fe–X'' and ''others'' were calculated with the {Fe–Fe, Fe–P, and Fe–O} and {P–P, P–O, and O–O} atom pairs, respectively. Notably, the contribution of H_2O was ignored in this calculation because of the dehydration of SB. The two distinguishable peaks of the bump and separated dispersion of the atomic correlations in the VV structure support the structural similarity between VV and SB (Fig. 5 and 6).

4. Conclusions

This study investigated the effects of the dehydration and deprotonation of coordinated H_2O molecules based on the Li intercalation in (partially oxidized) VV and SB. Regarding the capacity and reaction rate, SB was a more appropriate active material than VV for Li intercalation. This feature was attributed to the higher total amount of Fe^{3+}, owing to the oxidation process accompanying the deprotonation. The higher reaction rate was due to the structural space created by dehydration. In terms of structural changes, Li intercalation did not induce the formation of any byproducts in the iron phosphates. Although the crystal structure of VV showed no significant changes, an increase in $Fe_3(PO_4)_2$ sheet separation and structural disorder were induced by Li intercalation. Additionally, the structural similarity between VV and SB was implied from the observed halo pattern of Li-intercalated VV and XRD patterns of Li-intercalated SB. This similarity is also supported by the discussion of the two peaks included in the bump of the XRD pattern of SB. More detailed work will be required for the structural analysis of Li-intercalated VV and SB. The oxidation state of the structure and porosity of materials could be controlled by deprotonation and degassing of a ligand if the framework structure, including multivalent metal elements, has organic ligands.

Author contributions

R.Y. conceived and designed the experiments. R.Y. and K.S. conducted the XANES and XRD measurements. R.Y. and H.L. conducted the electrochemical reactions. R.Y. wrote the manuscript with contributions from H.L., K.S., and T.I. All authors discussed the data interpretation.

Conflicts of interest

There are no conflicts to declare.

Acknowledgements

The authors would like to thank Ms Toshiko Itagaki (Analytical Research Core for Advanced Materials, Institute for Materials Research, Tohoku University) for the ICP-AES analysis and Dr Fumiaki Wakiyama for providing private communication on the original idea of this experiment. This research was supported by JSPS KAKENHI (Grant No. JP22K14750, JP20H00189, and JP18H05456).

Notes and references

1 A. Manthiram, A reflection on lithium-ion battery cathode chemistry, *Nat. Commun.*, 2020, **11**, 1–9.
2 Y. Arnaud, E. Sahakian, J. Lenoir, A. Roche and J. C. Charbonnier, Study of hopeite coatings, *Appl. Surf. Sci.*, 1988, **32**, 296–308.
3 K. Kobayashi, H. Ohtsu, T. Wada, T. Kato and K. Tanaka, Characterization of a stable ruthenium complex with an oxyl radical, *J. Am. Chem. Soc.*, 2003, **125**, 6729–6739.
4 D. O. Whittemore and D. Langmuir, Standard electrode potential of $Fe^{3+} + e^- = Fe^{2+}$ from 5–35C, *J. Chem. Eng. Data*, 1972, **17**, 288–290.
5 H. Hongu, A. Yoshiasa, G. Kitahara, Y. Miyano, K. Han, K. Momma, R. Miyawaki, M. Tokuda and K. Sugiyama, Crystal structure refinement and crystal chemistry of parasymplesite and vivianite, *J. Mineral. Petrol. Sci.*, 2021, **116**, 183–192.
6 H. Shao, N. Padmanathan, D. McNulty, C. O'Dwyer and K. M. Razeeb, Supercapattery based on binder-free $Co_3(PO_4)_2 \cdot 8H_2O$ multilayer nano/microflakes on nickel foam, *ACS Appl. Mater. Interfaces*, 2016, **8**, 28592–28598.
7 F. Capitelli, G. Chita, M. R. Ghiara and M. Rossi, Crystal-chemical investigation of $Fe_3(PO_4)_2 \cdot 8H_2O$ vivianite minerals, *Z. Krist.*, 2012, **227**, 92–101.
8 D. Rouzies and J. M. M. Millet, Mössbauer study of synthetic oxidized vivianite at room temperature, *Hyperfine Interact.*, 1993, **77**, 19–28.
9 G. Amthauer and G. R. Rossman, Mixed valence of iron in minerals with cation clusters, *Phys. Chem. Miner.*, 1984, **11**, 37–51.
10 C. A. McCammon and R. G. Burns, The oxidation mechanism of vivianite as studied by Mössbauer spectroscopy, *Am. Mineral.*, 1980, **65**, 361–366.
11 D. Hanzel, W. Meisel, D. Hanzel and P. Gütlich, Mössbauer effect study of the oxidation of vivianite, *Solid State Commun.*, 1990, **76**, 307–310.
12 R. L. Frost, R. Scholz, X. Ruan and R. M. F. Lima, A thermogravimetric, scanning electron microscope and vibrational spectroscopic study of the phosphate mineral santabarbaraite from Santa Barbara mine, Tuscany, Italy, *J. Therm. Anal. Calorim.*, 2016, **124**, 639–644.
13 K. Chiba, M. Takahashi, E. Ohshima, T. Kawamata and K. Sugiyama, The synthesis of metavivianite and the oxidation sequence of vivianite, *J. Mineral. Petrol. Sci.*, 2020, **115**, 485–489.
14 K. Momma and F. Izumi, VESTA 3 for three-dimensional visualization of crystal, volumetric and morphology data, *J. Appl. Crystallogr.*, 2011, **44**, 1272–1276.
15 S. Brindusoiu, M. Poienar, C. N. Marin, P. Sfirloaga, P. Vlazan and I. Malaescu, The electrical conductivity of $Fe_3(PO_4)_2 \cdot 8H_2O$ materials, *J. Mater. Sci.: Mater. Electron.*, 2019, **30**, 15693–15699.

16 A. H. Narten, Diffraction pattern and structure of noncrystalline bef2 and SiO_2 at 25 °C, *J. Chem. Phys.*, 1972, **56**, 1905–1909.
17 K. Sugiyama, Y. Waseda and S. Kudo, Structural analysis of hydrolytic condensed zirconium oxide by the anomalous X-ray scattering method, *ISIJ Int.*, 1991, **31**, 1362–1367.
18 Y. Waseda, K. Sugiyama and J. M. Toguri, Direct determination of the local structure in molten alumina by high temperature X-ray diffraction, *J. Z. Naturforsch. A*, 1995, **50a**, 770–774.
19 N. W. Thomas, A new approach to calculating powder diffraction patterns based on the Debye scattering equation, *Acta Crystallogr., Sect. A: Found. Crystallogr.*, 2010, **66**, 64–77.